Full Paper
doi.org/10.1002/chem.202003793

|Hot Paper|

( )- - 3 4 - 4- N

Shasha Dou[+],[a] Shuqing Zhou[+],[a] Hexiu Huang,[a] Puxuan Yan,[a] Elvis Shoko,[b] Tayirjan Taylor Isimjan,*[c] and Xiulin Yang*[a]

Developing a bifunctional catalyst with low cost and high catalytic performance in $NaBH_4$ hydrolysis for H_2 generation and selective reduction of nitroaromatics will make a significant impact in the field of sustainable energy and water purification. Herein, a low-loading homogeneously dispersed Pd oxide-rich Co_3O_4 polyhedral catalyst (PdO-Co_3O_4) with concave structure is reported by using a metal–organic framework (MOF)-templated synthesis method. The results show that the PdO-Co_3O_4 catalyst has an exceptional turnover frequency (3325.6 mol_{H2} min^{-1} mol_{Pd}^{-1}), low activation energy (43.2 kJ mol^{-1}), and reasonable reusability in catalytic H_2 generation from $NaBH_4$ hydrolysis. Moreover, the optimized catalyst also shows excellent catalytic performance in the $NaBH_4$ selective reduction of 4-nitrophenol to 4-aminiphenol with a high first-order reaction rate of approximately 1.31 min^{-1}. These excellent catalytic properties are mainly ascribed to the porous concave structure, monodispersed Pd oxide, as well as the unique synergy between PdO and Co_3O_4 species, which result in a large specific surface area, high conductivity, and fast solute transport and gas emissions.

Metal–organic frameworks (MOFs) are attracting significant attention in the field of material science because of their high surface area, tunable porosities, and specific coordinated metal centers.[1] Additionally, these unique features also lead to the potential application of MOFs as pyrolysis precursors for various heterogeneous catalysts.[2] Depending upon the pyrolysis and post-treatment conditions, MOF precursors could result in bulk or supported composites bearing extraordinary catalytic performances.[3] This type of MOF-templated synthesis (MOFTS), generally performed either under air or inert atmosphere, leads to highly dispersed metal species encapsulated by a porous carbon matrix thereby minimizing catalyst sintering. Notably, the MOF carbonization under an inert environment at high temperatures often results in highly porous carbon cages that are capable of hosting well-dispersed metal species.[4] As a result, not only is the electrical conductivity of these materials improved compared with similar composites prepared under air, but also the electrical interaction between various components is enhanced. Therefore, the main current applications of MOFTS catalysts are mostly focused on electrochemical research, including electrochemical water splitting, energy storage, and energy conversion, where the enhanced electrical properties play an important role.[5] Moreover, recent progress on the MOFTS technique has been extended to the field of heterogeneous composite catalysis because of the excellent compatibility of MOFs with both organic and inorganic materials. This work has led to the synthesis of a wide range of nanocomposites achieving diverse spatial morphologies and catalytic activities.[6] Nevertheless, most of the works are focused on a single functional catalyst. Multifunctional catalysts prepared through MOFTS methods have not yet been widely studied. However, progress in this direction is now emerging in bifunctional catalysts. For example, Zhang et al. synthesized a unique 3D hierarchical rod-like structure by using a MOF template that exhibited better electrocatalytic activities for oxygen reduction and oxygen evolution reactions (ORR and OER, respectively) than that of commercial Pt/C and RuO_2, respectively. Additionally, the rechargeable Zn-air batteries based on their catalyst showed initial charge and discharged potentials at 1.81 and

[a] S. Dou,[+] S. Zhou,[+] H. Huang, P. Yan, Prof. Dr. X. Yang
Guangxi Key Laboratory of Low Carbon Energy Materials
School of Chemistry and Pharmaceutical Sciences
Guangxi Normal University, Guilin 541004 (China)
E-mail: xlyang@gxnu.edu.cn

[b] Dr. E. Shoko
Department of Chemistry, University of Liverpool, Liverpool L69 3BX (UK)

[c] Dr. T. T. Isimjan
Saudi Arabia Basic Industries Corporation (SABIC) at
King Abdullah University of Science and Technology (KAUST)
Thuwal 23955-6900 (Saudi Arabia)
E-mail: isimjant@sabic.com

[+] These authors contributed equally to this work.

Supporting information and the ORCID identification number(s) for the author(s) of this article can be found under: https://doi.org/10.1002/chem.202003793.

1.28 V (2 mA cm^{-2}), along with excellent cycling stability.[5] As usual, the focus is still on the electrochemistry.

The MOFTS catalysts also show remarkable performance for hydrogen production from $NaBH_4$ hydrolysis. Although hydrogen is considered the most promising clean energy source of the 21st century, there are still major barriers to its large-scale adoption related to its safe transportation and storage.[7] $NaBH_4$ has been extensively investigated as a hydrogen storage material because of its low molecular weight, high hydrogen content (10.57 wt%), and high stability in solution.[8] Meanwhile, there are reports showing that the MOFTS catalysts can also catalyze nitrophenols (NPs) to aminophenols (APs).[9] As carcinogenic pollutants, NPs are extremely toxic to the environment, and they have a devastating effect on the kidney, liver, and the central nervous system of both animals and humans.[10] Conversion of NPs to some other useful intermediate chemicals such as APs is always highly desired. The most effective approach to reducing NPs is to use catalytic $NaBH_4$ reduction.[11] There are mainly three types of nano-catalysts used in this process, including noble metals,[12] non-noble metals,[13] and carbon materials.[14] To the best of our knowledge, there is no report on the bifunctional feature of MOFTS catalysts, where it can be used both in $NaBH_4$ hydrolysis and NPs reduction.

Setting this goal in our mind, we developed a concave structure of Pd oxide-decorated Co_3O_4 polyhedra (PdO-Co_3O_4) with low Pd loading (0.9 wt% Pd) by using a MOFTS method. This was followed by a controllable two-step calcination treatment. The crystal structure, microscopic morphology, .2(t9(.)](maj)68.9C29.3416Tm[(T)99.vasteer)-362.1(of)-358.8(the)530.4(compl in

4-

$PdO\text{-}Co_3O_4$ catalyst (15 mg), water (9.5 mL), ethanol (8 mL), and 4-nitrophenol (70 mg) were mixed in one pot, a 50 mL beaker, to form a homogeneous solution by magnetic stirring (600 rpm). The reaction started immediately after 4.0 $NaBH_4$ solution (0.5 mL) was added into the beaker at 298 K. The progress of the reaction was monitored by taking 1 mL samples from the reaction mixture at various time intervals. For each sample, CH_2Cl_2 (5 mL) and ethanol (2 mL) were immediately added, followed by dilution of the solution with water 20 times before testing by UV/Visible spectroscopy.

The first-order reaction rate (k) was calculated as follows [Eq. (3)]:[16]

$$k \quad \ln\left(\frac{c_t}{c_0}\right)/t \qquad 3$$

in which c_t/c_0 is the ratio of the concentration after t time to the initial concentration, replaced by the intensity ratio of the ultraviolet absorption spectrum, and t is the time.

A schematic diagram of the preparation of the concavely structured porous $PdO\text{-}Co_3O_4$ polyhedron is shown in Figure 1a. The Pd-Co-MOF composite is obtained by simple solvothermal aging of the cobalt nitrate, palladium acetylacetone, and 2-MI precursors in methanol, where the Pd species are evenly distributed throughout the frameworks. Through a controlled heating rate and an optimized calcination temperature, during the pyrolysis of the MOF in an inert atmosphere, Pd and Co species undergo partial reduction, thereby obtaining the Pd-Co-CN composite. After further air oxidation treatment, the nitrogen–carbon species were removed, and the Pd-Co species were oxidized to construct the targeted porous $PdO\text{-}Co_3O_4$ polyhedron with abundant oxygen defects.

X-ray diffraction (XRD) patterns are used to explore the crystal structure of the materials. As shown in Figure 1b, the diffraction peaks indicated by the $PdO\text{-}Co_3O_4$ composite are consistent with the cubic structure of Co_3O_4 (JCPDS: 74–1657).[17] Still, the presence of PdO species is not detected owing to the low content of PdO. Raman spectroscopy was then used to further explore the microstructure of the $PdO\text{-}Co_3O_4$ composite. Figure 1c shows five Raman active modes at 179, 463, 507, 598, and 668 cm ^{1}, which are lower than the reported pure spinel structure of Co_3O_4 materials at about 15–25 cm ^{1}.[18] This phenomenon may be a reflection of the strong interaction between Co and Pd species in the composite, which is also detected by X-ray photoelectron spectroscopy (XPS).

Scanning electron microscopy (SEM) images were used to investigate the changes in the morphology of materials at differ-

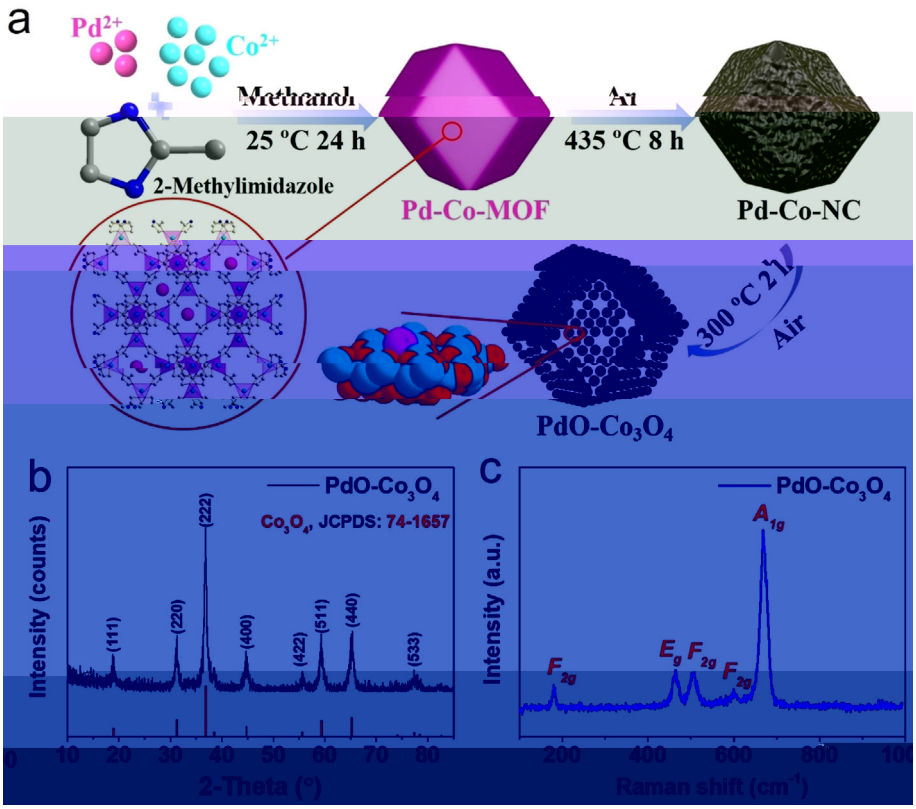

1. (a) Schematic diagram of the synthesis of concavely structured $PdO\text{-}Co_3O_4$ polyhedra. (b) XRD patterns and (c) Raman spectrum of $PdO\text{-}Co_3O_4$.

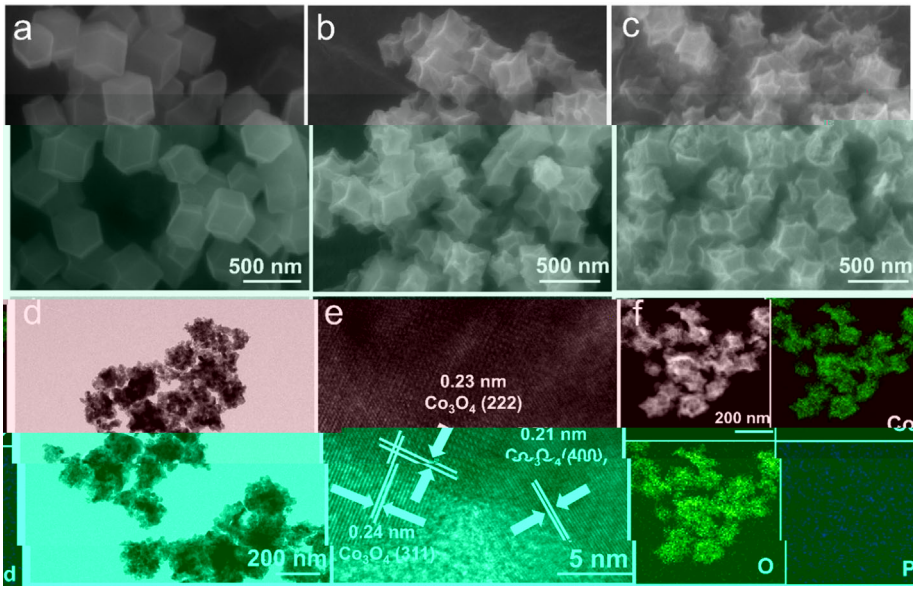

2. SEM images of (a) Pd-Co-MOF, (b) Pd-Co-NC, and (c) PdO-Co_3O_4. (d) TEM and (e) high-resolution TEM images of PdO-Co_3O_4. (f) HAADF-STEM image of PdO-Co_3O_4 and corresponding element mappings of Co, O, Pd.

ent stages of transformation. As shown in Figure 2a, the synthesized Pd-Co-MOF has a rhombic dodecahedron structure with an average size of about 420 nm (Figure S1 in the Supporting Information), and its crystal structure is consistent with ZIF-67 (Figure S2 in the Supporting Information).[19] After carbonization at 435 °C in Ar atmosphere, the surface of the regular dodecahedron of the MOF collapsed and the volume decreased to an average size of approximately 320 nm (Figure 2b). At the same time, the Co species was reduced to metallic Co clusters (Figure S3 in the Supporting Information)[20] as the Pd-Co-NC phase formed. Thermogravimetric analysis (TGA) was used to track the pyrolysis process of Pd-Co-MOF in Ar gas (Figure S4 in the Supporting Information). Significant weight loss for the MOF occurred above 435 °C; this may be undesirable as excessive weight loss is reported to lead to metal agglomeration.[21] Accordingly, we performed all the calcinations under Ar atmosphere at 435 °C to reduce the risk of metal agglomeration. Subsequent calcination in air revealed that the carbon species could be rapidly removed by burning at temperatures higher than 229 °C (Figure S5 in the Supporting Information). Therefore, to ensure complete elimination of the carbon species, we performed all calcinations in air at 300 °C. The corresponding PdO-Co_3O_4 powders maintained a similar pre-calcined morphology, but the average particle size further decreased to about 290 nm (Figure 2c).

Transmission electron microscopy (TEM) was used to further observe the microstructure of PdO-Co_3O_4 powders (Figure 2d). The high-resolution TEM image of the PdO-Co_3O_4 nanocrystals shown in Figure 1e shows two distinct crossed lattice fringes with a plane spacing of 0.23 nm and 0.24 nm, which are attributed to the (222) and (311) planes of Co_3O_4, respectively.[22] The lattice spacing of 0.21 nm corresponds to the (400) crystal plane of Co_3O_4.[23] As shown in Figure S6 (in the Supporting Information), the energy-dispersive X-ray (EDX) spectrum of PdO-Co_3O_4 confirms the existence of Pd, Co, and O elements. The high angle annular dark field (HAADF)-STEM and the elemental mappings show that Pd, Co, and O elements are evenly distributed in the framework structure of the PdO-Co_3O_4 composite (Figure 2f). We further investigated the textural features of the PdO-Co_3O_4 powders by N_2 adsorption/desorption isotherms and observed a type III isotherm (Figure S7 in the Supporting Information). The Brunauer–Emmett–Teller (BET) surface area of the PdO-Co_3O_4 powders was 67.3 $m^2 g^{-1}$, and the pore size distribution was about 38 nm. The porous structure helps to expose more active sites and to enhance the mass transfer, that is, solute transport and product release from the surface.

XPS was used to analyze the surface chemical state and composition of the PdO-Co_3O_4 powder. Figure S8a (in the Supporting Information) shows that the PdO-Co_3O_4 polyhedron is mainly composed of Co, O, and C elements, where the Pd signal intensity is weak owing to the low content. The high-resolution XPS spectra of the C1s regions (Figure S8b in the Supporting Information) are deconvoluted into C=C (284.0 eV), C–C (284.8 eV), and C–O (286.0 eV) and used as a calibration standard.[24] Figure 3a is the high-resolution Co2p spectra of PdO-Co_3O_4 and Co_3O_4. The Co $2p_{3/2}$ region of the PdO-Co_3O_4 polyhedron is deconvoluted into four peaks at 779.4, 780.9, 785.0, and 789.4 eV, corresponding to the Co^{3+}, Co^{2+}, and two satellite peaks, respectively.[23,25] It can be seen that a small number of coexisting Pd species makes the area ratio of Co^{3+}/Co^{2+} markedly increase from 2.46 to 3.12. The high-resolution O1s spectra of the two samples were further analyzed in Figure 3b, in which three signals generated at 529.4, 530.7, and 532.0 eV are attributed to metal oxides, oxygen vacancies, and adsorbed H_2O, respectively.[26] It is worth mentioning that the

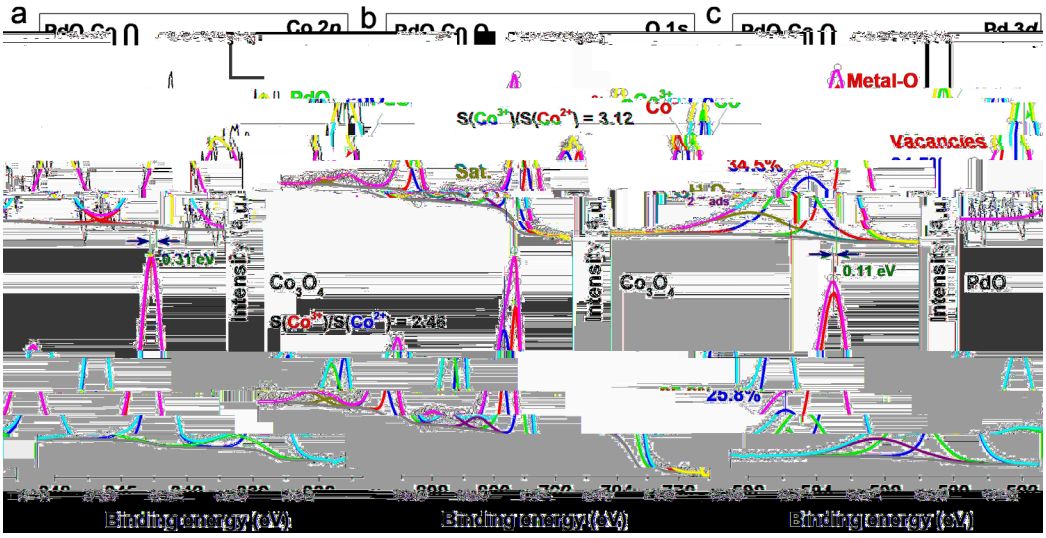

3. High-resolution XPS spectra of (a) Co 2p and (b) O 1s regions of PdO-Co_3O_4 and Co_3O_4, (c) Pd 3d regions of PdO-Co_3O_4 and commercial PdO powders.

oxygen vacancies increased rapidly from 25.8% to 34.5% after the introduction of Pd species. Studies indicate that a higher proportion of oxygen vacancies corresponds to faster electron transfer, stronger adsorption properties, and more active sites.[27]

The high-resolution Pd 3d spectrum was analyzed by fitting two asymmetric peaks (Figure 3c). The fitted Pd $3d_{5/2}$ and Pd $3d_{3/2}$ peaks located at 337.1 eV and 342.3 eV are attributed to PdO.[28] Compared with commercial PdO, it can be found that the Pd $3d_{5/2}$ peak in PdO-Co_3O_4 moved by 0.31 eV owing to the electron transfer from Co species to Pd species, resulting in higher electron density on PdO species.[29,31] As the content of Co_3O_4 in PdO-Co_3O_4 is much higher than that of PdO, almost no change in Co 2p is observed. The strong electronic interaction between different species will affect the adsorption, transformation, and desorption capabilities of active sites, thereby synergistically improving the catalytic activity. Notably, this strong interaction may be unique to the PdO-Co_3O_4 composite as no such shift was observed when we used a similar method to replace Co with Zn to construct PdO_x-ZnO (Figure S9 in the Supporting Information).

The catalytic H_2 production from the hydrolysis of $NaBH_4$ in alkaline solution was performed at 25 °C by employing an experimental setup schematically illustrated in Figure S10 (in the Supporting Information). The amount of H_2 produced was calculated based on the volume of water discharged by H_2. Figure 4a–b shows the comparison of the catalytic hydrolysis of $NaBH_4$ by PdO-Co_3O_4 materials prepared from the calcination of Pd-Co-NC at different temperatures in air. We can observe that, of the three samples, the PdO-Co_3O_4 catalyst prepared by calcination at 300 °C yields both the highest HGR (6300.5 $mL_{H2}\,min^{-1}\,g_{cat}^{-1}$) and TOF (3325.6 $mol_{H2}\,min^{-1}\,mol_{Pd}^{-1}$). We emphasize that this TOF value is the largest ever reported to the best of our knowledge. Among the highest TOF values we found in the literature are included Ni_2Pt@ZIF-8,[30] Co-Ru-P@NF,[31] and $Ni_{0.9}Pt_{0.1}/Ce_2O_3$.[32] In Figure 4c, we explore the effect of Pd loading on the rate of hydrogen evolution. It can be seen that the highest HGR and TOF values are obtained at 0.9 wt% Pd loading (Figure 4d and Table S1 in the Supporting Information). The somewhat counterintuitive poor catalytic performance at higher Pd loading probably results from increased particle agglomeration, which in turn reduces the overall surface area. As the best catalytic performance was obtained for the PdO-Co_3O_4 calcined in air at 300 °C with 0.9 wt% Pd loading, unless stated otherwise, our discussion of PdO-Co_3O_4 will focus on this sample henceforth.

To investigate the effects of the different components of the PdO-Co_3O_4 catalyst on H_2 generation by $NaBH_4$ hydrolysis, we explored PdO-Co_3O_4 alongside Pd-Co-NC, PdO_x-ZnO, and Co_3O_4 control catalysts (Figure 5a). The results show that none of the individual components of the PdO-Co_3O_4 catalyst system exhibit any meaningful catalytic activity, clearly demonstrating that the observed outstanding catalytic activity of PdO-Co_3O_4 must at least be grounded in the synergy between its PdO and Co_3O_4 components (Figure 5b). To further explore the influence of different precious metals, we used similar methods to prepare two other catalysts, PtO_x and RuO_2 decorated Co_3O_4 catalysts (Figure 5c). It can be seen that the catalytic activity of PdO-Co_3O_4 is significantly higher than those of the two control catalysts and most previously reported catalysts (Figure 5d and Table S2 in the Supporting Information). These variations in catalytic performance could be related to differences in the chemical interactions among the constituents of the different catalysts. We also explored the impact of both the concentration of $NaBH_4$ and the percentage of NaOH on the H_2 generation by the $NaBH_4$ hydrolysis reaction. In line with previous studies,[15a] we find no important role for these variables on the HGR (Figure S11 in the Supporting Information).

The temperature dependence of the catalytic activities was investigated in the range 298–318 K. We can clearly observe a gradual increase of the H_2 generation rate of the PdO-Co_3O_4

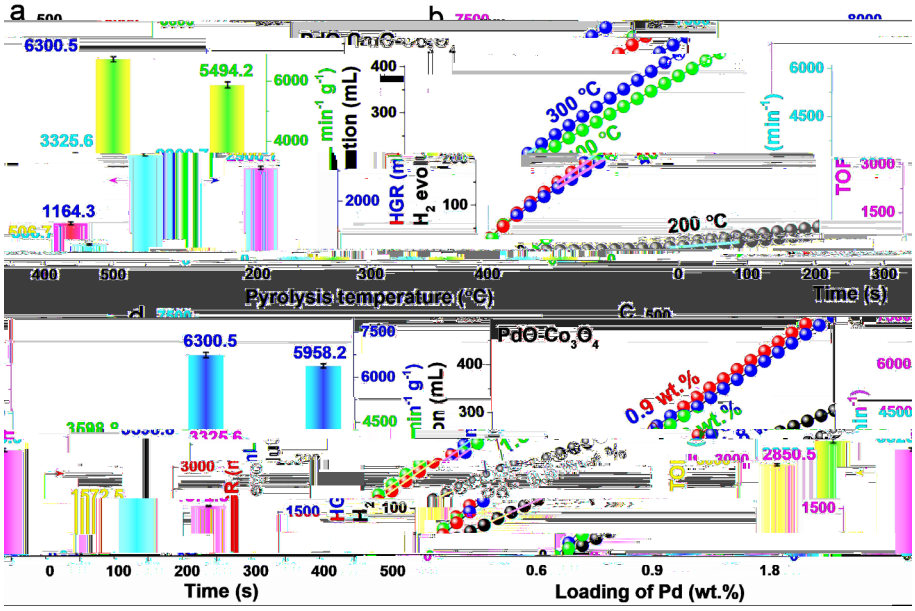

4. (a) Stoichiometric H_2 evolution and (b) the summarized TOF and HGR values by PdO-Co_3O_4 catalysts with different pyrolysis temperatures. (c) Relationship between H_2 evolution and loadings of Pd species in PdO-Co_3O_4 catalysts, and (d) Summarized TOF values and HGR. All the experiments were conducted in 150 mL $NaBH_4$+0.4 wt% NaOH solution at 25 °C.

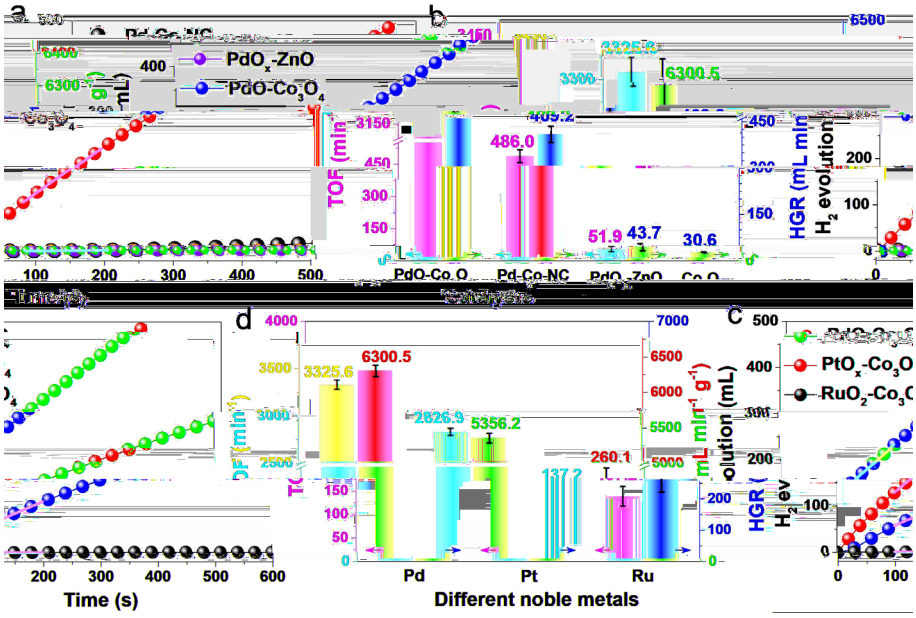

5. (a) Stoichiometric H_2 evolution and (b) the summarized TOF and HGR values of different catalysts. (c) Relationship between H_2 generation and different noble metal catalyst decorated Co_3O_4 and (d) summarized TOF values and HGR. All the experiments are conducted in 150 mL $NaBH_4$+0.4 wt% NaOH solution at 25 °C.

catalyst with increasing reaction temperature (Figure 6a). From the Arrhenius plots in Figure 6b, the activation energies of the PdO-Co_3O_4 and PdO-Co_3O_4 (air) catalysts are calculated to be 43.2 and 52.0 kJ mol^{-1}, respectively. Here, the PdO-Co_3O_4 (air) refers to Figure S12 (in the Supporting Information). The significantly lower activation energy obtained for the PdO-Co_3O_4 catalyst indicates an enhanced catalytic activity.[33] The recycling test was used to evaluate the catalyst reusability. After the complete consumption of $NaBH_4$, a fresh $NaBH_4$ powder sample was then added to the reactor for the next cycle (Figure 6c). The horizontal axis in Figure 6c is the running time for the experiment showing the instances at which each cycle was initiated. The results show that the H_2 production starts immediately and maintains high activity without a significant induction period. This test cycle was repeated five times, and around 80% of the initial activity was retained after five cycles

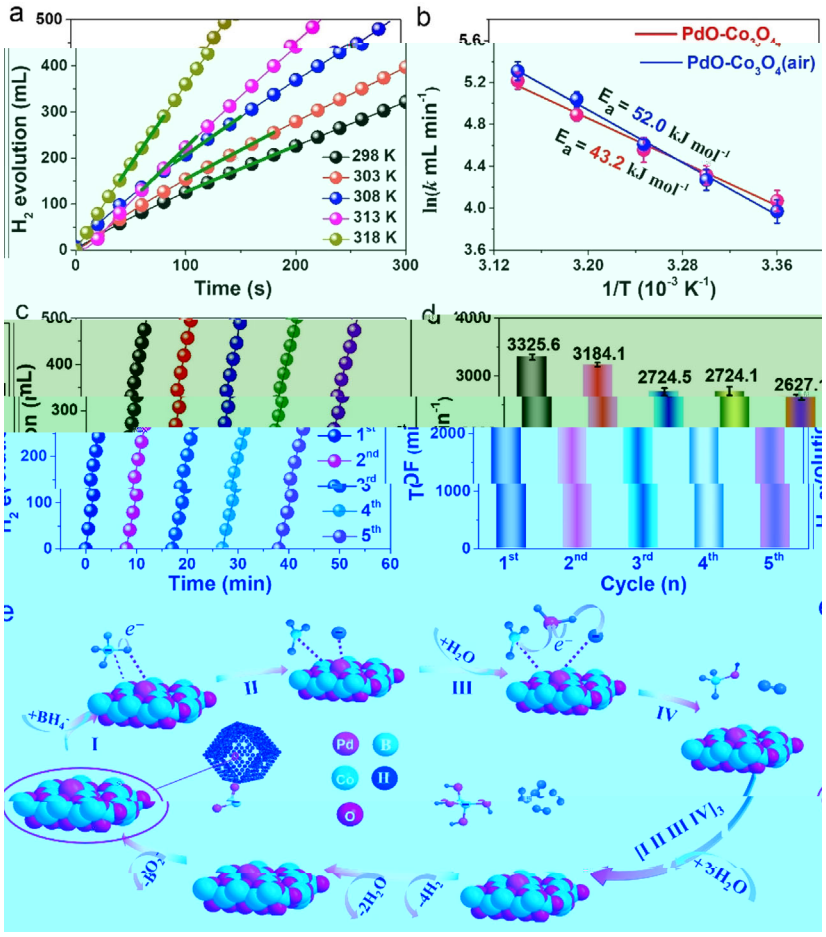

. (a) Stoichiometric H_2 evolution of PdO-Co_3O_4 and PdO-Co_3O_4 (air) in 150 m NaBH$_4$+0.4 wt% NaOH solution at different reaction temperatures and (b) the summarized Arrhenius plots from (a). (c) Recycling stability test of PdO-Co_3O_4 catalyst and (d) the corresponding TOF values from (c). (e) Proposed catalytic mechanism of PdO-Co_3O_4 catalyst for H_2 generation.

(Figure 6d). The slight decrease in catalytic activity may be mainly due to the structural damage (Figure S13 in the Supporting Information), Pd clusters exfoliation (Table S1 in the Supporting Information), surface chemical state changes (Figure S14 in the Supporting Information), and BO_2^- poisoning.[29a,34]

As discussed above, the PdO-Co_3O_4 catalyst has the largest HGR and TOF values compare with other catalysts. The outstanding performance is mainly attributed to a large specific surface area, high conductivity, and synergy between PdO and Co_3O_4 species. According to the XPS study, the negative shift of the Pd 3d binding energy in PdO-Co_3O_4 caused by the partial electron transfer from Co species to Pd species indicates a higher electron density on Co species compared with that of Pd species. Accordingly, the partially negatively charged hydrogen atoms preferred to attach to the Pd atoms. As a result, the BH_4^- dissociates at the Co and Pd metal sites, hydrogen atoms are adsorbed on Pd, and BH_3 is attached to Co species. After the B–H bond is broken, the negatively charged B species immediately transfers the negative charge to the adsorbed H atoms through the conductive bulk. Finally, the negatively charged H atom on the Pd surface extracts hydrogen from water to release an H_2 molecule, whereas the OH^- ion attacks the BH_3 to form a BH_3OH molecule, followed by transfer of one hydrogen atom of the BH_3OH to a free Pd site. After the first cycle, the surface of the catalyst releases a hydrogen molecule and a BH_3OH species. As the reaction proceeds, all of the H atoms in the borohydride are replaced by OH^- ions (Figure 6e), ultimately releasing the $B(OH)_4^-$ species.[35]

4-

Since Pal et al. first reported the reduction of 4-NPs to 4-APs by using a Ag catalyst in 2002, the reaction has become a well-controlled model reaction that does not produce byproducts.[11] Thus, we selected this model reduction reaction in an aqueous system with $NaBH_4$ as the hydrogen source to study the catalytic efficiency of the PdO-Co_3O_4 polyhedron (Figure 7a). The reaction was monitored at the specific UV wavelength.[36] After adding $NaBH_4$ to 4-NP, the solution was observed to turn bright yellow with the absorption peak shifting to about 405 nm; however, we noticed no further changes in color after 1 h, indicating that the 4-nitrophenol ion was formed.[16b,37] After further addition of the PdO-Co_3O_4 catalyst, the UV/Vis absorption peak decreased rapidly, demonstrating that 4-nitrophenol ions were reduced to 4-aminophenol ions (Fig-

ure 7b and Figure S15 in the Supporting Information). As shown in Figure 7c, we observed that the PdO-Co_3O_4 (0.9 wt% Pd) catalyst needs only about 220 s to complete the full conversion of 4-NP to 4-AP. This is a much faster rate compared with commercial 10 wt% Pd/C or 20 wt% Pt/C catalysts for the same initial 4-NP concentration. Furthermore, the kinetic constants of PdO-Co_3O_4 catalysts were calculated according to the slope of ln(

electron transfer $NaBH_4$ hydrolysis nitrophenol reduction $PdO\text{-}Co_3O_4$ synergistic effect

[1] H. Park, S. Oh, S. Lee, S. Choi, M. Oh, *Appl. Catal. B* **201** , *246*, 322 – 329.
[2] A. Muthurasu, V. Maruthapandian, H. Y. Kim, *Appl. Catal. B* **201** , *248*, 202 – 210.
[3] S. Lee, S. Oh, M. Oh, *Angew. Chem. Int. Ed.* **2020**, *59*, 1327 – 1333; *Angew. Chem.* **2020**, *132*, 1343 – 1349.
[4] C. Van Nguyen, S. Lee, Y. G. Chung, W.-H. Chiang, K. C. W. Wu, *Appl. Catal. B* **201** , *257*, 117888.
[5] M. Zhang, Q. Dai, H. Zheng, M. Chen, L. Dai, *Adv. Mater.* **201** , *30*, 1705431.
[6] J. Ying, J. Li, G. Jiang, Z. P. Cano, Z. Ma, C. Zhong, D. Su, Z. Chen, *Appl. Catal. B* **201** , *225*, 496 – 503.
[7] a) S. Demirci, A. K. Sunol, N. Sahiner, *Appl. Catal. B* **2020**, *261*, 118242; b) J. Lai, B. Huang, Y. Chao, X. Chen, S. Guo, *Adv. Mater.* **201** , *31*, 1805541.
[8] a) G. Bozkurt, A. Özer, A. B. Yurtcan, *Energy* **201** , *180*, 702 – 713; b) J. Guo, B. Wang, D. Yang, Z. Wan, P. Yan, J. Tian, T. T. Isimjan, X. Yang, *Appl. Catal. B* **2020**, *265*, 118584; c) L. Shi, Z. Chen, Z. Jian, F. Guo, C. Gao, *Int. J. Hydrogen Energy* **201** , *44*, 19868 – 19877.
[9] a) S. M. Sadeghzadeh, R. Zhiani, S. Emrani, *New J. Chem.* **201** , *42*, 988 – 994; b) L. Jin, X. Zhao, J. Ye, X. Qian, M. Dong, *Catal. Commun.* **201** , *107*, 43 – 47.
[10] a) M. I. Din, R. Khalid, Z. Hussain, T. Hussain, A. Mujahid, J. Najeeb, F. Izhar, *Crit. Rev. Anal. Chem.* **2020**, *50*, 322 – 338; b) G. Eichenbaum, M. Johnson, D. Kirkland, P. O'Neill, S. Stellar, J. Bielawne, R. DeWire, D. Areia, S. Bryant, S. Weiner, D. Desai-Krieger, P. Guzzie-Peck, D. C. Evans, A. Tonelli, *Regul. Toxicol. Pharmacol.* **200** , *55*, 33 – 42.
[11] N. Pradhan, A. Pal, T. Pal, *Colloids Surf. A* **2002**, *196*, 247 – 257.
[12] a) F. Coccia, L. Tonucci, D. Bosco, M. Bressan, N. d'Alessandro, *Green Chem.* **2012**, *14*, 1073 – 1078; b) R. Liu, S. M. Mahurin, C. Li, R. R. Unocic, J. C. Idrobo, H. Gao, S. J. Pennycook, S. Dai, *Angew. Chem. Int. Ed.* **2011**, *50*, 6799 – 6802; *Angew. Chem.* **2011**, *123*, 6931 – 6934.
[13] a) Y. Sun, L. Xu, Z. Yin, X. Song, *J. Mater. Chem. A* **2013**, *1*, 12361 – 12370; b) C. Tang, F. Qu, A. M. Asiri, Y. Luo, X. Sun, *Inorg. Chem. Front.* **201** , *4*, 659 – 662.
[14] X.-H. Li, X. Wang, M. Antonietti, *Chem. Sci.* **2012**, *3*, 2170 – 2174.
[15] a) L. Cui, Y. Xu, L. Niu, W. Yang, J. Liu, *Nano Res.* **201** , *10*, 595 – 604; b) Q. Yao, Z.-H. Lu, Y. Yang, Y. Chen, X. Chen, H.-L. Jiang, *Nano Res.* **201** , *11*, 4412 – 4422.
[16] a) X. Cheng, D. Wang, J. Liu, X. Kang, H. Yan, A. Wu, Y. Gu, C. Tian, H. Fu, *Nanoscale* **201** , *10*, 22348 – 22356; b) Y. Yang, K. Jiang, J. Guo, J. Li, X. Peng, B. Hong, X. Wang, H. Ge, *Chem. Eng. J.* **2020**, *381*, 122596.
[17] a) Y. Sun, Y. Zhou, C. Zhu, W. Tu, H. Wang, H. Huang, Y. Liu, M. Shao, J. Zhong, S.-T. Lee, Z. Kang, *Appl. Catal. B* **201** , *244*, 795 – 801; b) S.-J. Choi, H.-J. Choi, W.-T. Koo, D. Huh, H. Lee, I.-D. Kim, *ACS Appl. Mater. Interfaces* **201** , *9*, 40593 – 40603.
[18] Y. Tong, H. Mao, Y. Xu, J. Liu, *Inorg. Chem. Front.* **201** , *6*, 2055 – 2060.
[19] a) X. C. Huang, Y. Y. Lin, J. P. Zhang, X. M. Chen, *Angew. Chem. Int. Ed.* **200** , *45*, 1557 – 1559; *Angew. Chem.* **200** , *118*, 1587 – 1589; b) H. Hu, B. Guan, B. Xia, X. W. Lou, *J. Am. Chem. Soc.* **2015**, *137*, 5590 – 5595.
[20] B. Coşkuner Filiz, A. Kantürk Figen, S. Pişkin, *Appl. Catal. B* **201** , *238*, 365 – 380.
[21] Y. Zhao, H. Zhou, W. Chen, Y. Tong, C. Zhao, Y. Lin, Z. Jiang, Q. Zhang, Z. Xue, W.-C. Cheong, B. Jin, F. Zhou, W. Wang, M. Chen, X. Hong, J. Dong, S. Wei, Y. Li, Y. Wu, *J. Am. Chem. Soc.* **201** , *141*, 10590 – 10594.
[22] a) H. Lee, X. Wu, Q. Ye, X. Wu, X. Wang, Y. Zhao, L. Sun, *Chem. Commun.* **201** , *55*, 1564 – 1567; b) H.-C. Li, Y.-J. Zhang, X. Hu, W.-J. Liu, J.-J. Chen, H.-Q. Yu, *Adv. Energy Mater.* **201** , *8*, 1702734.
[23] J. Huang, Y. Xiao, Z. Peng, Y. Xu, L. Li, L. Tan, K. Yuan, Y. Chen, *Adv. Sci.* **201** , *6*, 1900107.
[24] Y. She, Z. Lu, W. Fan, S. Jewell, M. K. H. Leung, *J. Mater. Chem. A* **2014**, *2*, 3894 – 3898.
[25] W. Chen, B. Han, C. Tian, X. Liu, S. Liang, H. Deng, Z. Lin, *Appl. Catal. B* **201** , *244*, 996 – 1003.
[26] a) J. Sun, N. Guo, Z. Shao, K. Huang, Y. Li, F. He, Q. Wang, *Adv. Energy Mater.* **201** , *8*, 1870121; b) S. Gao, F. Liao, S. Ma, L. Zhu, M. Shao, *J. Mater. Chem. A* **2015**, *3*, 16520 – 16527.
[27] Y. Tong, P. Chen, M. Zhang, T. Zhou, L. Zhang, W. Chu, C. Wu, Y. Xie, *ACS Catal.* **201** , *8*, 1 – 7.
[28] a) T.-J. Wang, F.-M. Li, H. Huang, S.-W. Yin, P. Chen, P.-J. Jin, Y. Chen, *Adv. Funct. Mater.* **2020**, *30*, 2000534; b) C. Wu, J. Guo, J. Zhang, Y. Zhao, J. Tian, T. T. Isimjan, X. Yang, *Renew. Energy* **201** , *136*, 1064 – 1070.
[29] B. Wang, H. Huang, M. Huang, P. Yan, T. T. Isimjan, X. Yang, *Sci. China Chem.* **2020**, *63*, 841 – 849.
[30] F. Fu, C. Wang, Q. Wang, A. M. Martinez-Villacorta, A. Escobar, H. Chong, X. Wang, S. Moya, L. Salmon, E. Fouquet, J. Ruiz, D. Astruc, *J. Am. Chem. Soc.* **201** , *140*, 10034 – 10042.
[31] J. Guo, C. Wu, J. Zhang, P. Yan, J. Tian, X. Shen, T. T. Isimjan, X. Yang, *J. Mater. Chem. A* **201** , *7*, 8865 – 8872.
[32] H.-L. Wang, J.-M. Yan, Z.-L. Wang, S.-I. Oh, Q. Jiang, *J. Mater. Chem. A* **2013**, *1*, 14957 – 14962.
[33] D. D. Tuan, K.-Y. A. Lin, *Chem. Eng. J.* **201** , *351*, 48 – 55.
[34] C. Wu, J. Zhang, J. Guo, L. Sun, J. Ming, H. Dong, Y. Zhao, J. Tian, X. Yang, *ACS Sustainable Chem. Eng.* **201** , *6*, 7451 – 7457.
[35] U. B. Demirci, P. Miele, *C. R. Chim.* **2014**, *17*, 707 – 716.
[36] M. Fan, W. D. Wang, Y. Zhu, X. Sun, F. Zhang, Z. Dong, *Appl. Catal. B* **201** , *257*, 117942.
[37] a) L. Tan, B. Tan, *Chem. Eng. J.* **2020**, *390*, 124485; b) E. Park, J. Jack, Y. Hu, S. Wan, S. Huang, Y. Jin, P.-C. Maness, S. Yazdi, Z. Ren, W. Zhang, *Nanoscale* **2020**, *12*, 2596 – 2602.
[38] Q. Sun, N. Wang, T. Zhang, R. Bai, A. Mayoral, P. Zhang, Q. Zhang, O. Terasaki, J. Yu, *Angew. Chem. Int. Ed.* **201** , *58*, 18570 – 18576; *Angew. Chem.* **201** , *131*, 18743 – 18749.
[39] B. Baruah, G. J. Gabriel, M. J. Akbashev, M. E. Booher, *Langmuir* **2013**, *29*, 4225 – 4234.

Manuscript received: August 15, 2020
Revised manuscript received: September 11, 2020
Accepted manuscript online: September 15, 2020
Version of record online: ■■ ■■, 0000

Full Paper
doi.org/10.1002/chem.202003793

S. Dou, S. Zhou, H. Huang, P. Yan, E. Shoko, T. T. Isimjan,* X. Yang*

■■ – ■■

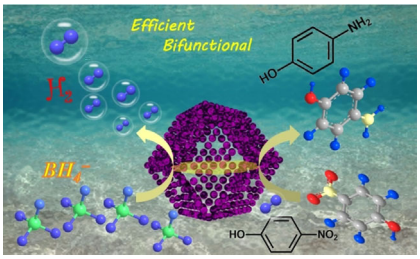

: A homogeneously dispersed Pd oxide-rich Co_3O_4 polyhedral catalyst with concave structure has been used as a highly active catalyst for $NaBH_4$ hydrolysis and 4-nitrophenol reduction. The excellent catalytic performance is attributed to the unique structure and the synergy between the PdO and Co_3O_4 species.